Physical Review & Research International
4(1): 9-29, 2014

SCIENCEDOMAIN *international*
www.sciencedomain.org

Ice-Shelf Resonance Deflections Modelled with a 2D Elastic Centre-Line Model

Y. V. Konovalov[1*]

[1]*Department of Mathematics, National Research Nuclear University "MEPhI", Kashirskoe shosse, 31, 115409, Moscow, Russian Federation.*

Author's contribution

The only author performed the whole research work. Author YVK wrote the first draft of the paper. Author YVK read and approved the final manuscript.

Research Article

Received 16th April 2013
Accepted 12th July 2013
Published 7th October 2013

ABSTRACT

Ice-shelf flexure modelling was performed using a 2D finite-difference elastic model, which takes into account sub-ice-shelf seawater flux. The sub-ice seawater flux was described by the continuity equation linked with the linear Euler equation. In the model ice shelf flexures result from variations in the incoming (outgoing) sea water flux, which flows into (out of) the sub-ice-shelf channel. The numerical experiments were carried out for the centre line, which passes from the summit to the glacier terminus along one of the fastest ice-stream at the Academy of Sciences Ice Cap. The profile includes a part of the adjacent ice-shelf. The numerical experiments were carried out for harmonic incoming seawater fluxes and the ice-shelf flexures were obtained for a wide spectrum of the seawater flux frequencies, ranging from tidal periods down to periods of a few tens of seconds (0.001..0.06 Hz). The solutions obtained by the model are in agreement (in amplitude of the flexures) with the ones obtained by the model of Holdsworth and Glynn (1978). The amplitudes of modelled ice-shelf deflections reach a maxima and it's in concordance with previous investigations of the impact of ocean waves on Antarctic ice shelves [1]. The explanation of the effect is found in the existence of a resonance at these high frequencies.

Keywords: Ice shelf; ocean waves; resonance deflections; sub-ice-shelf seawater; 2D elastic model.

[*]*Corresponding author: Email: yu-v-k@yandex.ru;*

1. INTRODUCTION

Tides and ocean swells produce ice shelf bends and, thus, they can initiate break-up of sea-ice in the marginal zone [2-7] and also they can lead to ice-shelf rift propagation. Strong correlations between rift propagation rate and ocean swells impact has however, yet to be revealed [8], and it is not clear to what degree rift propagation can potentially be triggered by tides and ocean swells. Nevertheless, the impact of tides and ocean swells is the part of the total force that produces sea ice calving processes in ice shelves. Nevertheless, the impacts of tides and of ocean swells are the parts of the total force [8] that produces sea-ice calving processes in ice shelves [9]. Thus, the understanding of vibrating processes in ice shelves is important from the point of view of investigations of ice sheet-ocean interactions and of sea level changes due to alterations in the rate of sea-ice calving.

The descriptions of ice-shelf bends and of ice-shelf vibrations were developed in [2,3,6,7,10] using the approximation of thin plates. These models allow to simulate ice-shelf deflections and to obtain bending stresses emerging due to the vibrating processes, and to assess possible effects of tides and ocean swells impacts on the calving process. Further development of elastic-beam models for description of ice-shelf flexures implies application of visco-elastic rheological models. In particular, tidal flexures of ice-shelf were obtained within linear visco-elastic Burgers model in [11].

Ice-stream response to ocean tides was described by full Stokes 2D finite-element employing a non-linear visco-elastic Maxwell rheological model by Gudmundsson (2011). This modelling work revealed that tidally induced ice-stream motion is strongly sensitive to the parameters of the sliding law. In particular, a non-linear sliding law allows the explanation of the ice stream response to ocean forcing at long-tidal periods (MSf) through a nonlinear interaction between the main semi-diurnal tidal components [12].

A 2D finite-element flow-line model with an elastic rheology was developed by O. V. Sergienko [1,13] and was used to estimate mechanical impact of high-freq tidal action on stress regime of ice shelves. In this model seawater was considered as incompressible, inviscid fluid and is described by a velocity potential.

Here the simulations of bends of ice shelves are performed by 2D finite-difference elastic model. The numerical experiments were carried out for the centre line, which passes along one of the four ice streams at the Academy of Sciences Ice Cap on the Komsomolets Island, Severnaya Zemlya archipelago [14]. The sub-ice-shelf seawater flux is described by the two equations: (1) the continuity equation and (2) the linear Euler equation. The main aim of this work is to derive equations and corresponding boundary conditions describing the impact of ocean wave action on ice shelves, and also to present a finite-difference model of the vibrating motion within the glacier, ice shelf and sub-ice-shelf sea system. The flexures/vibration of ice shelves are considered in the model as a response to alterations of the incoming seawater flux. In turn, the alterations of seawater flux are caused by changes in sea level. Ice shelf flexures were obtained by the model for a wide spectrum of frequencies of the seawater flux fluctuations. The modelled ice shelf flexures are compared with the thin plate flexures obtained by the Holdsworth & Glynn model (1978).

2. THE 2D FINITE-DIFFERENCE ELASTIC MODEL

2.1 Field Equations

The 2D model is based on the well-known momentum equations that can be applied to a vertical cross-section along a flow line (centre line) [15-18]:

$$\begin{cases} \dfrac{\partial \sigma_{xx}}{\partial x}+\dfrac{\partial \sigma_{xz}}{\partial z}=\rho\dfrac{\partial^2 U}{\partial t^2}; \\ \dfrac{\partial \sigma_{zx}}{\partial x}+\dfrac{\partial \sigma_{zz}}{\partial z}=\rho g+\rho\dfrac{\partial^2 W}{\partial t^2}; \\ 0<x<L;\ h_b(x)<z<h_s(x). \end{cases} \tag{1}$$

where (x,z) is a rectangular coordinate system with the *x* axis along the central line and the *z* axis pointing vertically upward; U, W are horizontal and vertical ice displacements, respectively; σ_{ik} is stress tensor; $h_b(x)$, $h_s(x)$ are ice bed and ice surface elevations, respectively; *L* is the glacier length.

Sub-ice-shelf seawater flux produces variation in pressure (P'), and gives rise to deviations from the hydrostatic pressure. The sub-ice seawater flux, which appears due to ice-shelf deviations, are described by the continuity equation and by the linear Euler equation:

$$\begin{cases} \dfrac{\partial W_b}{\partial t}=\dfrac{\partial}{\partial x}(d_0(x)\ v); \\ \dfrac{\partial v}{\partial t}=-\dfrac{1}{\rho_w}\dfrac{\partial P'}{\partial x}; \\ 0<x<L. \end{cases} \tag{2}$$

where $d_0(x)$ is the depth of the sub-ice-shelf channel, $W_b(x,t)$ is the ice-shelf base vertical deflection, $v(x)$ is the horizontal velocity of the sub-ice-shelf seawater flow.

2.2 Boundary Conditions

The boundary conditions are (a) stress free ice surface, (b) normal stress exerted by seawater at the ice shelf terminus and at the ice-shelf base, (c) basal stress defined by friction law at glacier bed, (d) zero values of horizontal displacement and of shear stress at the ice sheet summit.

The general form of the friction law [12,19] is expressed as

$$\tau_i \, \sigma_{ik} \, n_k = K_{fr} \left| \vec{\mu}_b \right|^{m-1} \left(\vec{\mu}_b \right)_i \tau_i \,, \tag{3}$$

where K_{fr} is friction coefficient, m is the exponent in the friction law, $m = 1$ gives linear friction law and $m > 1$ corresponds to non-linear friction law; $\vec{\mu}_b$ is the base ice flow velocity; $\vec{\tau}$ and $\vec{n}$ are tangential and normal to the bed vectors, respectively.

The base ice flow velocity $\vec{\mu}_b$ and the friction coefficient K_{fr} are considered as given parameters of the elastic model. In this manuscript the ice flow velocity $\vec{\mu}_b$ and the friction coefficient K_{fr} were taken from [20].

Boundary conditions for sub-ice-shelf water flow, which is described by Eq (2), are

(i) $v = 0$ and $W_b = 0$ at $x = 0$;

(ii) $\dfrac{\partial W_b}{\partial t} = \dfrac{\partial}{\partial x}\left(d_0(x) \, v \right)$ and $v(t) = v_0(t)$ at $x = L$;

2.3 Discretization of the Model

The numerical solutions were obtained by a finite-difference method, which based on the coordinate transformation $x, z \to x, \xi = \left(h_s - z \right) / H$ [21-28]. The coordinate transformation transfigures a cross-section into the rectangle $\Pi = \left\{ 0 \le x \le L; 0 \le \xi \le 1 \right\}$.

To provide stability of the numerical solution in the finite-difference method, the boundary conditions have been included in the momentum equations (1) [20]. In particular, after the coordinate transformation, the boundary conditions for the system of momentum equations (1) at the upper glacier surface (free surface) can be written as

$$\begin{cases} \left(\dfrac{\partial \sigma_{xx}}{\partial x} \right)^1 + \left(\xi'_x \dfrac{\partial \sigma_{xx}}{\partial \xi} \right)^1 + \dfrac{1}{H} \dfrac{d h_s}{d x} \dfrac{1}{\Delta \xi} \sigma_{xx}^1 - \dfrac{1}{H} \dfrac{1}{\Delta \xi} \sigma_{xz}^2 = \rho \left(\dfrac{\partial^2 U}{\partial t^2} \right)^1; \\ \left(\dfrac{\partial \sigma_{xz}}{\partial x} \right)^1 + \left(\xi'_x \dfrac{\partial \sigma_{xz}}{\partial \xi} \right)^1 + \dfrac{1}{H} \dfrac{d h_s}{d x} \dfrac{1}{\Delta \xi} \sigma_{xz}^1 - \dfrac{1}{H} \dfrac{1}{\Delta \xi} \sigma_{zz}^2 = \rho \, g + \rho \left(\dfrac{\partial^2 W}{\partial t^2} \right)^1; \end{cases} \tag{4}$$

where the index "1" indicates that corresponding terms are approximated in grid nodes that located at ice surface and the index "2" corresponds to next sub-ice-surface grid layer, $\Delta \xi$ is vertical grid size.

The boundary conditions at the ice-shelf base differ from Eq (2) due to the hydrostatic pressure, which acts to ice-shelf base, and are given by

$$\begin{cases} \left(\frac{\partial \sigma_{xx}}{\partial x}\right)^{N_\xi} + \left(\xi'_x \frac{\partial \sigma_{xx}}{\partial \xi}\right)^{N_\xi} - \frac{1}{H}\frac{1}{\Delta\xi}\frac{d h_b}{d x}\sigma_{xx}^{N_\xi} + \frac{1}{H}\frac{1}{\Delta\xi}\sigma_{xz}^{N_\xi - 1} = \\ \qquad = \frac{1}{\Delta\xi}\frac{d h_b}{d x}\rho g + \frac{1}{H}\frac{1}{\Delta\xi}\frac{d h_b}{d x}P' + \rho\left(\frac{\partial^2 U}{\partial t^2}\right)^{N_\xi}; \\ \left(\frac{\partial \sigma_{xz}}{\partial x}\right)^{N_\xi} + \left(\xi'_x \frac{\partial \sigma_{xz}}{\partial \xi}\right)^{N_\xi} - \frac{1}{H}\frac{1}{\Delta\xi}\frac{d h_b}{d x}\sigma_{xz}^{N_\xi} + \frac{1}{H}\frac{1}{\Delta\xi}\sigma_{zz}^{N_\xi - 1} = \\ \qquad = \rho g - \frac{1}{\Delta\xi}\rho g - \frac{1}{H}\frac{1}{\Delta\xi}P' + \rho\left(\frac{\partial^2 W}{\partial t^2}\right)^{N_\xi}. \end{cases} \tag{5}$$

Where index "N_ξ" corresponds to grid layer located at the ice shelf base, P' is the deviation from the hydrostatic pressure in the sub-ice-shelf seawater.

The boundary conditions at the ice-shelf front after applying the finite differencing in the horizontal direction can be written in the following form

$$\begin{cases} -\frac{1}{\Delta x_{N_x-1}}(\sigma_{xx})_{N_x-1} + \left(\xi'_x \frac{\partial \sigma_{xx}}{\partial \xi}\right)_{N_x} = -\frac{1}{\Delta x_{N_x-1}} f(\xi) + \rho\left(\frac{\partial^2 U}{\partial t^2}\right)_{N_x}; \\ -\frac{1}{\Delta x_{N_x-1}}(\sigma_{xz})_{N_x-1} - \left(\frac{1}{H}\frac{\partial \sigma_{zz}}{\partial \xi}\right)_{N_x} = \rho g + \rho\left(\frac{\partial^2 W}{\partial t^2}\right)_{N_x}; \end{cases} \tag{6}$$

where $f(\xi) = \begin{cases} 0, & \xi < h_s/H; \\ \rho_w g(h_s - \xi H), & \xi \geq h_s/H. \end{cases}$ and index "N_x" corresponds to grid layer located at the ice-shelf front.

2.4 Equations for the Displacements

Constitutive relationships between stress tensor components and displacements correspond to Hook's law [17]:

$$\begin{cases} \sigma_{xx} = \frac{E}{(1+\nu)(1-2\nu)}\left\{(1-\nu)\left(\frac{\partial U}{\partial x} + \xi'_x \frac{\partial U}{\partial \xi}\right) - \nu \frac{1}{H}\frac{\partial W}{\partial \xi}\right\}; \\ \sigma_{zz} = \frac{E}{(1+\nu)(1-2\nu)}\left\{-(1-\nu)\frac{1}{H}\frac{\partial W}{\partial \xi} + \nu\left(\frac{\partial U}{\partial x} + \xi'_x \frac{\partial U}{\partial \xi}\right)\right\}; \\ \sigma_{xz} = \frac{E}{2(1+\nu)}\left\{-\frac{1}{H}\frac{\partial U}{\partial \xi} + \frac{\partial W}{\partial x} + \xi'_x \frac{\partial W}{\partial \xi}\right\}. \end{cases} \tag{7}$$

Substitution of these relationships into Eq (1), Eq (3) - (6) gives final equations of the model.

3. RESULTS OF THE NUMERICAL EXPERIMENTS

The numerical experiments with ice-shelf bends were carried out for the harmonic flux of inflowing/outflowing seawater and were applied to the centre line, which passes along the one of the four fast flowing ice streams at the Academy of Sciences Ice Cap [14] (Fig. 1). The C-C' profile [14] was continued into the ice-shelf profile using an idealized trapezoidal geometry for ice-shelf [3]. The ice shelf length, together with sub-ice-shelf channel depth $d_0(x)$, are considered as the model's parameters (Fig. 1).

It is assumed that incident ocean waves induce cyclical ice-shelf deflections that provide the cyclical circulation in the flux of sub-ice-shelf seawater. Thus, the boundary condition for Eq (2) can be formulated for the velocity of the incoming seawater flux:

$$v(L,t) = v_0 \sin \omega t \,, \tag{8}$$

where ω is the frequency of the incident ocean wave and v_0 is and the amplitude of the seawater flux velocity.

3.1 Tidal Waves

Ice-shelf response to the incoming seawater flux depends on the amplitude of the seawater flux velocity v_0, i.e. the response depends on the overall seawater flux incoming to sub-ice-shelf channel. For a given model's parameters including x-distribution of ice-shelf thickness, ice-shelf length (L_{sh}), Young's modulus and Poisson's ratio, the amplitude of seawater flux velocity should be chosen properly in order to provide the agreement between the amplitude of ice-shelf terminus deflection and the amplitude of incident ocean wave. Table 1 shows the ice-shelf length (L_{sh}) versus the amplitude of seawater flux velocity, at which the amplitude of ice-shelf terminus deflection achieves 1 m.

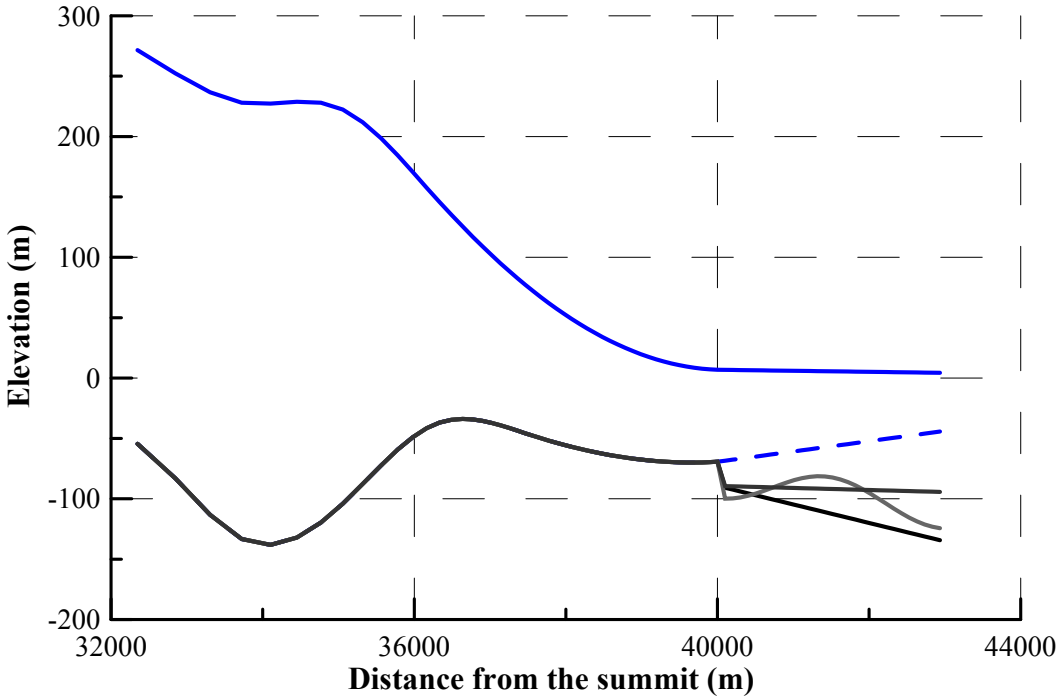

Fig. 1. The part of the C-C' profile, which passes in one of the four ice-streams in the Academy of Sciences Ice Cap (along the flow line) [14]. The C-C' also means one of the four flow lines in the Academy of Sciences Ice Cap (Figure 10 of Dowdeswell et al., 2002) The numerical experiments were carried out for the full C-C' profile, which extends from the ice sheet summit to the margin (Figure 8 of Dowdeswell et al., 2002). The C-C' profile was continuously converted into the ice-shelf, which has trapezoidal shape. The linear x-distributions of the depth of sub-ice-shelf channel and the linear x-distribution perturbed by a sinusoidal function, were considered in the numerical experiments. The ice shelf thickness is about 76.2 m at the distance where the grounding line located

Table 1. Ice-shelf lengths versus amplitude of seawater flux velocity. $E = 9\ GPa$, $\nu = 0.33$ **[29]**

L_{sh} (km)	2	3	4	5	6	7	8
v_0 (mm/s)	3.3	4.5	5.6	6.5	7.5	8.4	9.5

Fig. 2 shows vertical ice-shelf deflections obtained by the developed model (Fig. 2a) and by the model of Holdsworth & Glynn (1978) (Fig. 2b) for incident tidal ocean wave. The models reveal a visible distinction in the results obtained for the tidal wave and for different ice shelf lengths. The difference is observed in the positions of the maxima in the deflection profiles. The deflection profile maximum in the full model shifts from the grounding line to the ice-shelf terminus (Fig. 2a), but the maximum becomes unchanged in the profiles obtained by the elastic beam model (Fig. 2b), which is based on the momentum equation of a thin plate

[3] and which is in agreement with the exact solution based on the same 1D momentum equation for an elastic beam of a constant thickness [6,10].

Linear relationships of the d_0 on the distance x in Eq (2) were considered in the model, i.e. the d_0 linearly increases from a value d_1 at the grounding line to a value d_2 at the ice-shelf front, that is $d_0(x) = d_1 + (\Delta d / L_{Sh})(x - L_{Gl})$, where L_{Gl} is glacier length. In addition to the linear distributions the sinusoidal distribution of the d_0 was considered, that is $d_0(x) = d_1 + (\Delta d / L_{Sh})(x - L_{Gl}) + d_3(-1 + \cos(2\pi(x - L_{Gl})/L_{Sh}))$. Practically, this distribution defines the bump, which is located at the sea bottom in the middle of the sub-ice-shelf cannel (Fig. 1).

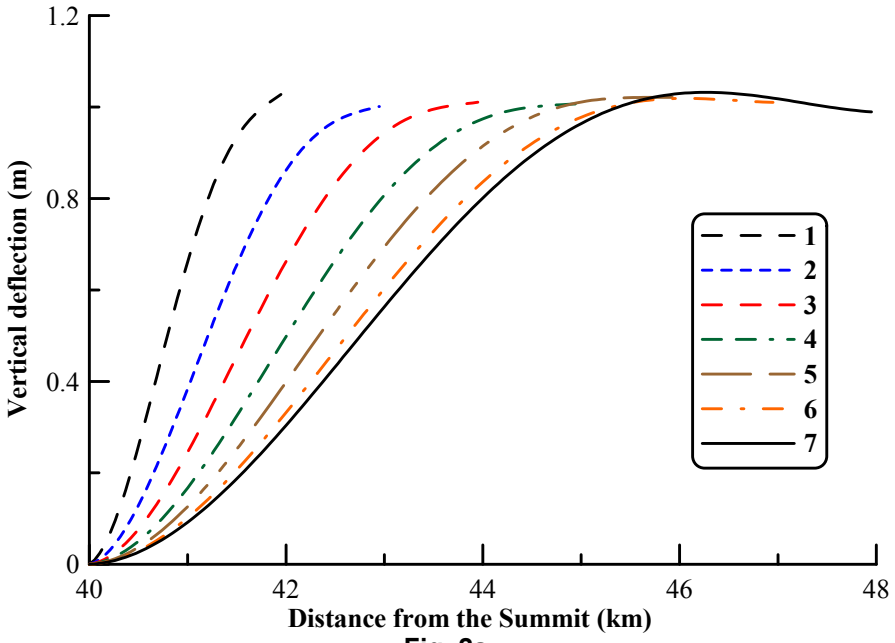

Fig. 2a

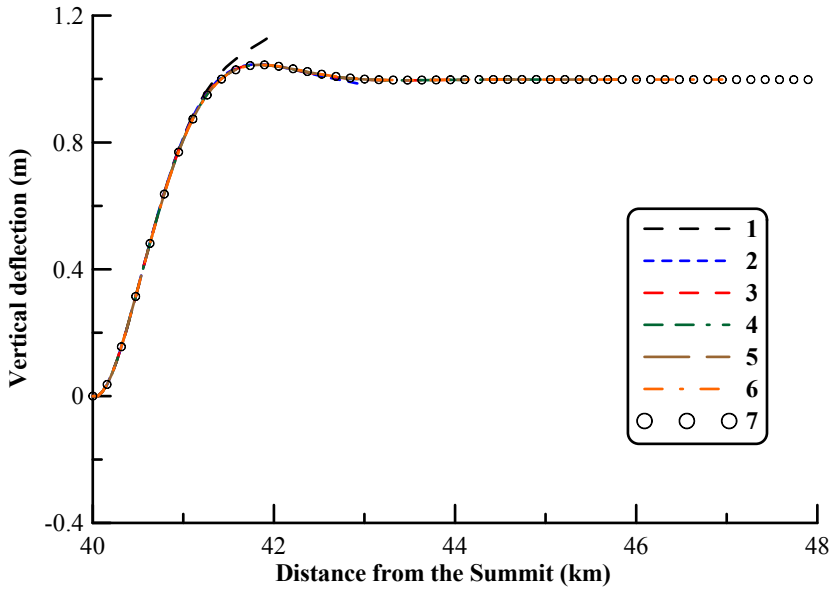

Fig. 2b

Fig. 2. ***(a)*** **The maximal ice-shelf deflections obtained by the full elastic model at different values of ice-shelf length: curves 1..8 corresponds to** $L_{Sh} = 2..8\,km$**, respectively.** ***(b)*** **The maximal ice-shelf deflections obtained by the model of Holdsworth & Glynn at the same values of ice-shelf length (and for the same trapezoidal geometries), i.e. curves 1..8 correspond to** $L_{Sh} = 2..8\,km$**, respectively. The modeled deflections are considered as deflections from the time-averaged flexure profile in the harmonic history of the forcing. Young's modulus** $E = 9\ GPa$ **, Poisson's ratio** $\nu = 0.33$ **, period of the vibrations** $T = 12\,h$ **(semi- diurnal periodicity), velocity amplitude of seawater flux is in the Table 1 and incoming wave amplitude in the model of Holdsworth & Glynn was taken equal to** $1\,m$ **.**

Fig. 3 shows that the increase in the coefficient of the linear distribution ($\Delta d / L_{Sh}$) leads to the enhancement of the ice-shelf deflections. In fact, Fig. 3 shows the overall incoming water flux impact to the amplitude of the deflections in the model, in the case when the amplitude of the flux velocity (v_0) in the incoming wave is considered as a given value. In this case the overall incoming water flux is defined by the value of d_2 (Fig. 3) and 1.5-times growing of d_2 means the same increase of the incoming water flux. In other words, the enhancement of the incoming water flux, which is defined as $\rho_w v_0 d_2$, will the same as the increase of d_2. The numerical experiment carried out with different values of the coefficient $\Delta d / L_{Sh}$ (Fig. 3) have revealed approximately the same-times growing of the deflection amplitude. That is the deflection amplitude growing in the agreement with the enhancement of the incoming water flux.

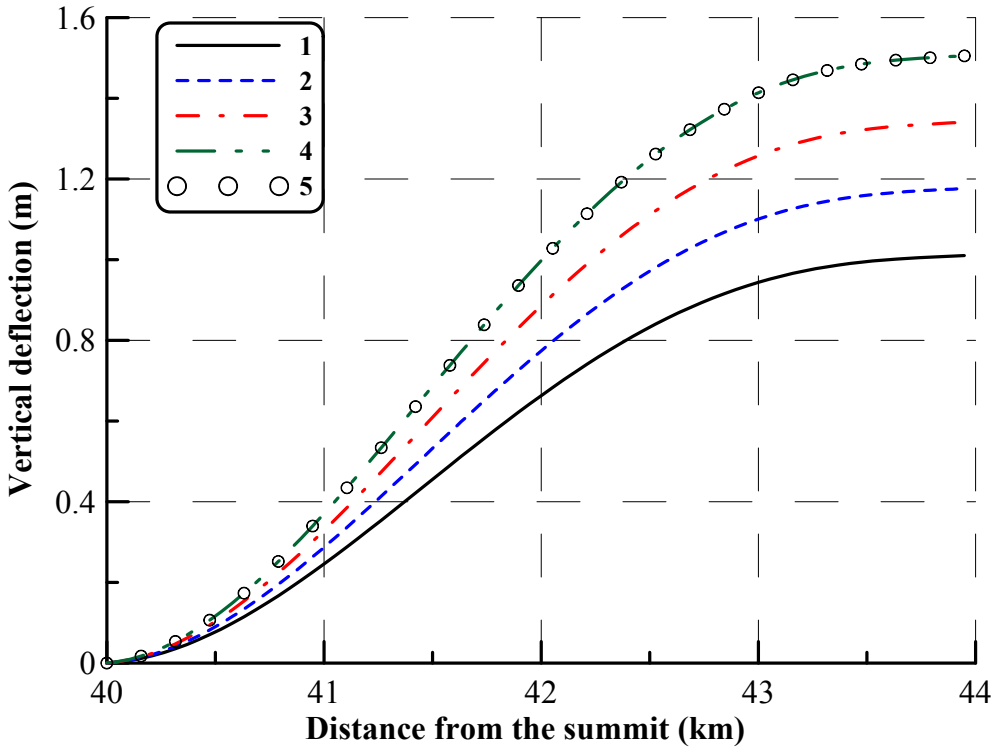

Fig. 3. Ice-shelf deflection profiles obtained by the full elastic model at different sub-ice-shelf channel depth profiles (Fig. 1). The curves 1-5 have been obtained at the linear depth distributions, i.e. $d_0(x)$ linearly changes from $d_1 = 30m$ to a value d_2: 1 - $d_2 = 60m$; 2 - $d_2 = 70m$; 3 - $d_2 = 80m$; 4 - $d_2 = 90m$. The curve 5 has been obtained at the sinusoidally perturbed sea bottom (Fig. 1). Young's modulus $E = 9\ GPa$, Poisson's ratio $\nu = 0.33$, period of the vibrations $T = 12\,h$ (semi- diurnal periodicity), amplitude of velocity of the incoming flux $v_0 = 5.6\,mm/s$

Fig. 4 shows velocity profiles of seawater flux (for the maximal flux) for linear seabed profile and for sinusoidally perturbed seabed profile (bumpy bed, Fig. 1), respectively. The profiles of $d_0(x)$ define the water velocity profiles so that the velocity profile takes the shape of the sea bed perturbations, respectively, but the deflections remain practically unchanged for the given set of model parameters (Fig. 3, curve 4 and curve 5).

The ice-shelf response to the semi-diurnal tidal wave, which is modulated by the wave with MSf-frequency [12], is shown in Fig. 5 and this response is in concordance with observed ice-shelf histories [8]. The ice-shelf response is symmetric unlike to the previous result obtained in the model based on the incoming pressure perturbations [30]. The symmetric response in the model is defined by equal inflowing and outflowing water fluxes in the water flux harmonic history, which is considered in the experiment (i.e. time-averaged water flux is equal to zero).

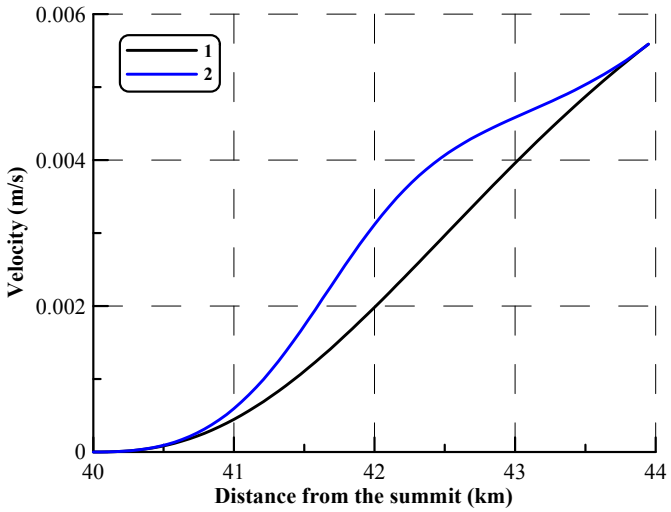

Fig. 4. Velocity profiles of the incoming water flux for linear seabed profile (curve 1) and for sinusoidal seabed profile (curve 2). The maximal velocities in the incoming water flux correspond respectively to the minimal ice-shelf deflection (which is equal to zero). Young's modulus $E = 9\ GPa$, Poisson's ratio $\nu = 0.33$, ice-shelf length $L_{sh} = 4\,km$, $v_0 = 5.6\,mm/s$

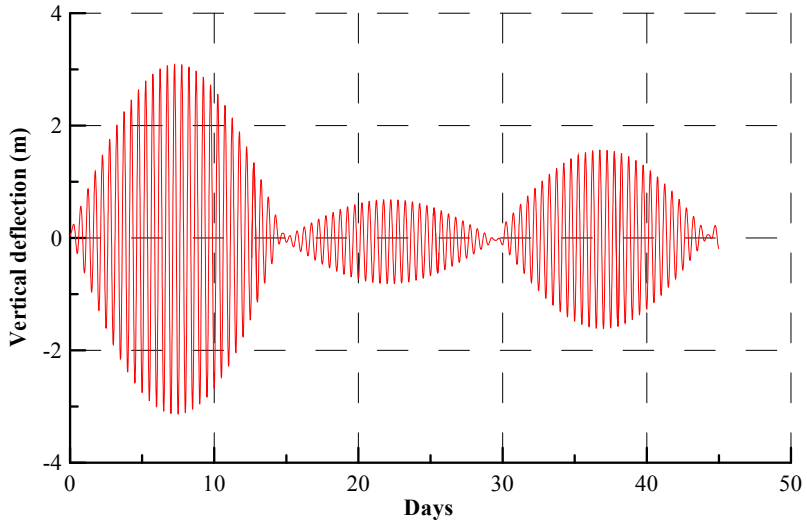

Fig. 5. The history of ice-shelf terminus deflection obtained for the semi-diurnal incident ocean wave, which is modulated by the wave with MSf frequency (14.76 days) [12]. The time interval covers three periods of the MSf component. The amplitudes of the flux velocity in the MSf component are equal to (i) $3v_0$ at the first period (ii) $0.7v_0$ at the second period and (iii) $1.5v_0$ at the third period, where $v_0 = 5.6\,mm/s$. Young's modulus $E = 9\ GPa$, Poisson's ratio $\nu = 0.33$, ice-shelf length $L_{sh} = 4\,km$.

3.2 Infragravity Waves (Response to High-Frequency Forcing)

Responses of the ice shelf to the harmonic incoming waves with higher frequencies ranging from 0.001 to 0.06 Hz, differs in a number of ways from the response at typical tidal frequencies of hours and days (Fig. 6). The main difference is that the amplitude of the ice-shelf deflections depends on the frequency of the forcing. The amplitude of the forcing, which is defined as the velocity amplitude of the incoming water flux, is considered as a given value, for example, is equal to 0.1 m/s, for all frequencies in the experiment (Fig. 6), but the amplitude of the ice-shelf terminus deflections ranging (a) from about 0.05 m (at 0.06 Hz) to about 0.9 m (at 0.011 Hz) for $L_{sh} = 2\,km$ (Fig. 7a), (b) from about 0.1 m (at 0.02 Hz) to about 1.5 m (at 0.0035 Hz) for $L_{sh} = 3\,km$ (Fig. 7b), (c) from about 0.1 m (at 0.06 Hz) to about 3 m (at 0.0016 Hz) for $L_{sh} = 4\,km$ (Fig. 7c).

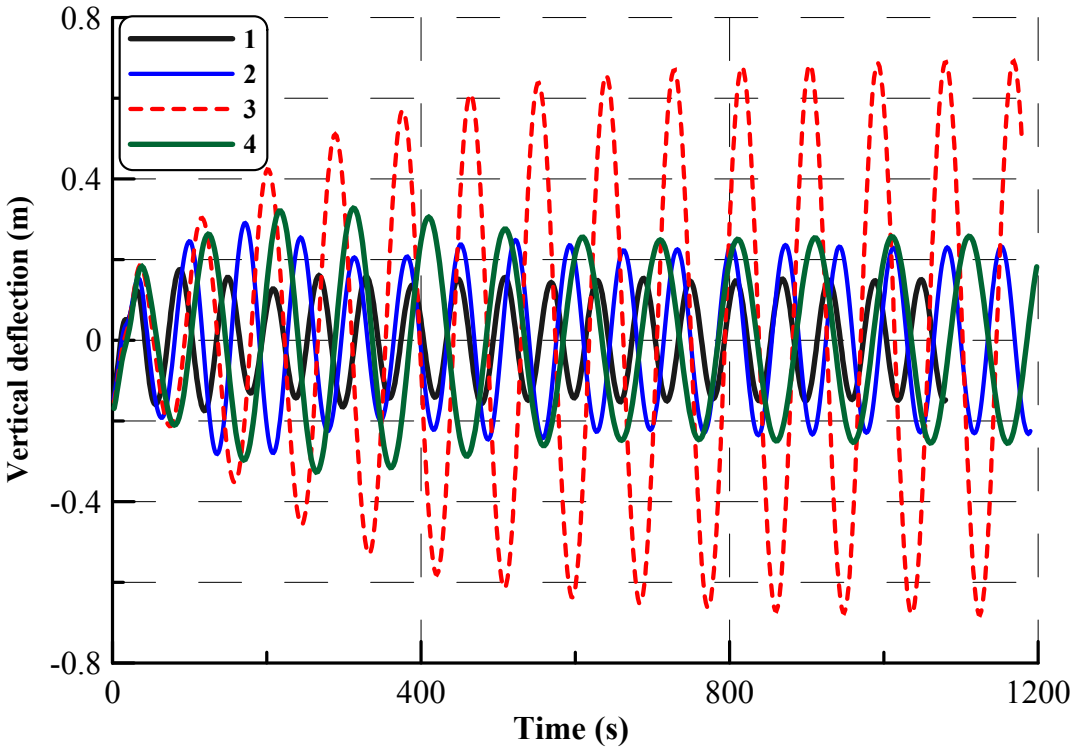

Fig. 6. The histories of ice-shelf terminus deflection obtained at the infragravity incident ocean waves [1]: 1 - $T = 60\,s$ **; 2 -** $T = 70\,s$ **; 3 -** $T = 88\,s$ **; 4 -** $T = 100\,s$ **. Young's modulus** $E = 9\ GPa$ **, Poisson's ratio** $\nu = 0.33$ **, incoming flux velocity amplitude** $v_0 = 0.1 m/s$

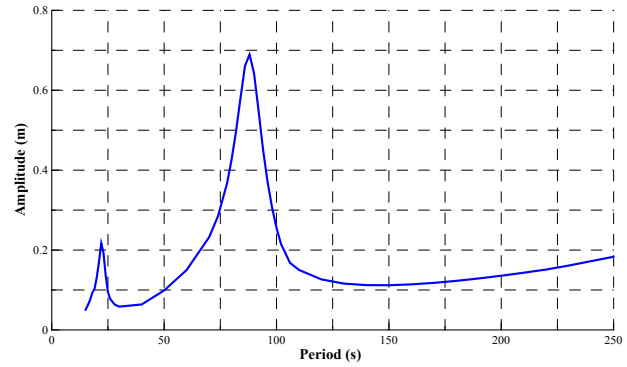

Fig. 7a

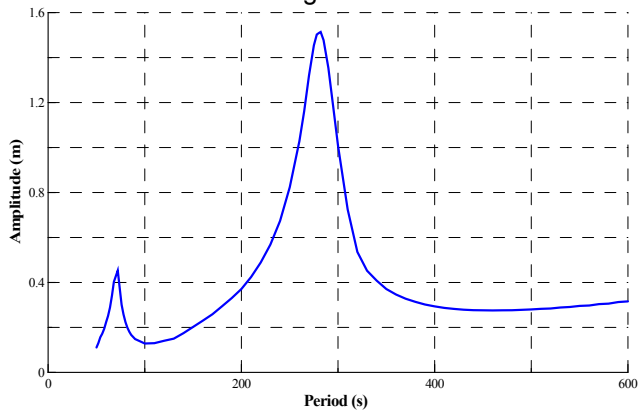

Fig. 7b

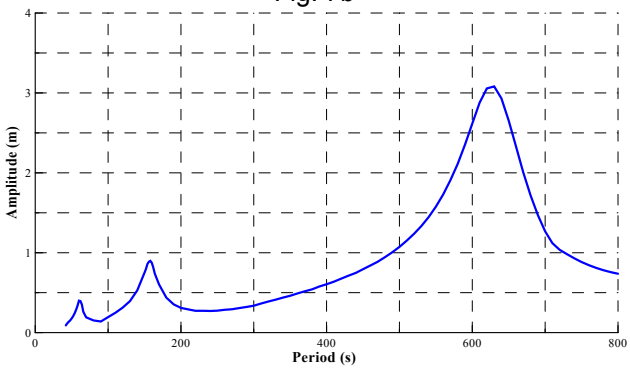

Fig. 7c

Fig. 7. Ice-shelf terminus deflection amplitude versus ocean wave frequency. The spectral distributions have been obtained for *(a)* $L_{sh} = 2\,km$, *(b)* $L_{sh} = 3\,km$, *(c)* $L_{sh} = 4\,km$. The considered frequencies ranging from 0.001 to 0.06 Hz. The maximum of the amplitude is reached in the first maximum (peak) at $T \approx 88\,s$ for $L_{sh} = 2\,km$, at $T \approx 282\,s$ for $L_{sh} = 3\,km$, and at $T \approx 630\,s$ for $L_{sh} = 4\,km$. Young's modulus $E = 9\ GPa$, Poisson's ratio $\nu = 0.33$, incoming flux velocity amplitude $v_0 = 0.1\,m/s$.

In other words, the spectral amplitude distribution, which reveals the resonance peaks, appears in the high-freq part of the ocean wave spectrum (Fig. 7). For a wide ocean wave spectrum, which begins from tidal frequencies and extends till the lower boundary of the high-frequencies (i.e. theoretically supposed that the spectrum is continuous), the ice-shelf deflection follows the incoming wave. "Follow" means that the amplitude of ice-shelf terminus deflection corresponds (approximately equals to) amplitude of the incoming wave. Generally speaking, water flux velocity in the model should depend on the frequency of the forcing. In practice, a constant value of the water flux velocity amplitude was used in the numerical experiments with high-freq forcing. Thus, we can observe monotonously increasing trends in the spectral amplitude distributions (Fig. 7). Nevertheless, the main difference of the high-freq part of the spectrum is the existence of the resonance peaks, some of which fall into the infragravity part of the spectrum [1].

Fig. 8 shows flexural ice-shelf profiles (waves in ice shelf) obtained by the model of Holdsworth & Glynn (1978) (Fig. 8a) and by the model developed here (Fig. 8b). The deflections obtained by the developed model are in agreement (in amplitude of the flexures) with the deflections obtained by the Holdsworth and Glynn model due to the fitting of the velocity of the incoming seawater flux. However, the positions of the nodes/antinodes and the eigen-frequencies are distinguished because the models differ in the field equations and in the sets of boundary conditions.

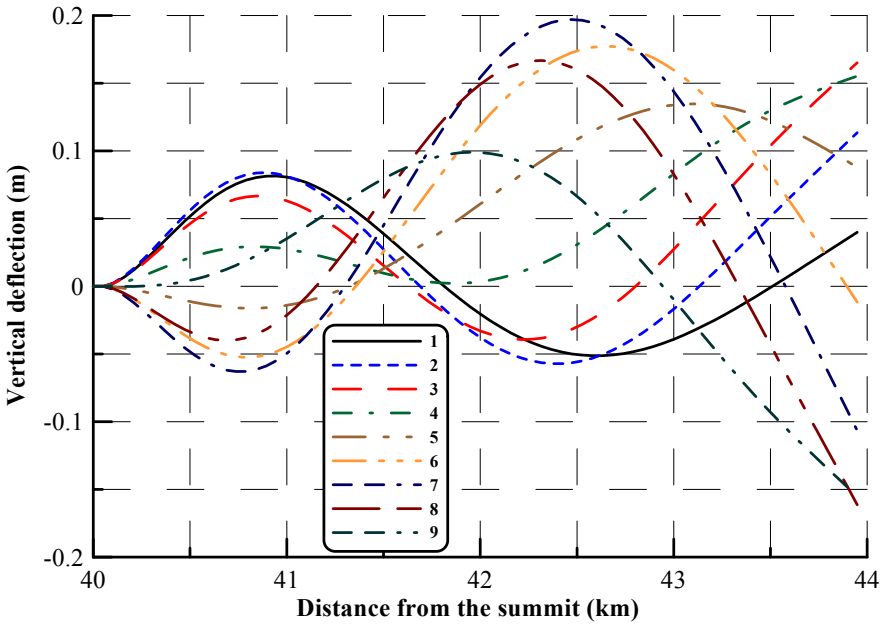

Fig. 8a

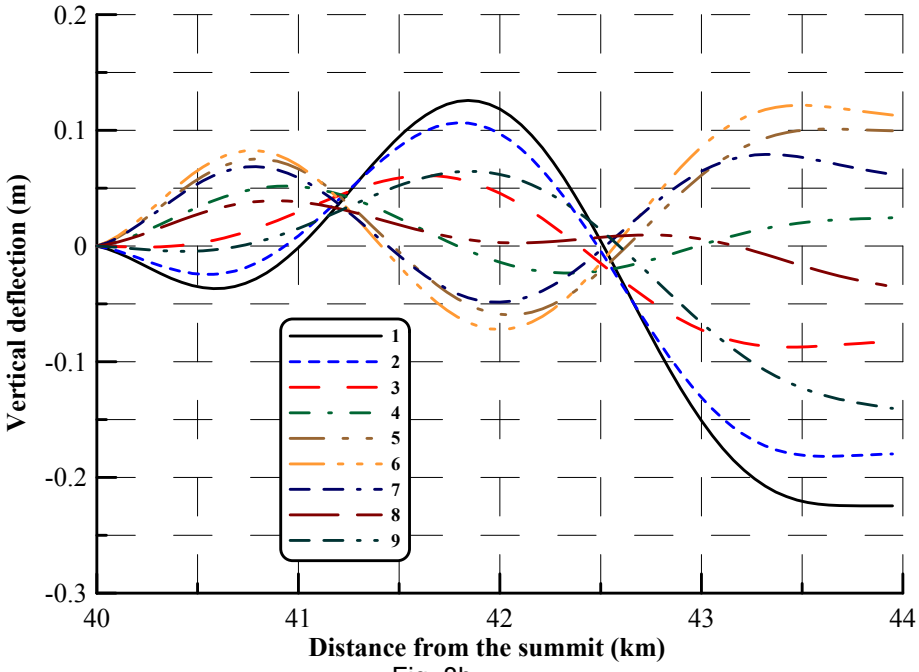

Fig. 8b

Fig. 8. Successive flexural ice-shelf profiles obtained by *(a)* the Holdsworth & Glynn model (1D elastic beam model); *(b)* by the full elastic model based on Eq. (1) - (2). Two successive curves are separated by the $\Delta t = T/10$ time step. The period T of the forcing is $T = 100\ s$. Ice-shelf length $L_{sh} = 4\,km$, Young's modulus $E = 9\ GPa$, Poisson's ratio $\nu = 0.33$, incoming wave amplitude in the Holdsworth & Glynn model $A = 0.3\,m$, incoming flux velocity amplitude in the full model $v_0 = 0.1\,m/s$

4. DISCUSSION

The modelled ice-shelf response has revealed that ice-shelf deflections are in agreement (in amplitude of the flexures) with the ones obtained by the model of Holdsworth & Glynn (1978) and in contrariety with preliminary results in [30]. Furthermore, the model, which based on Eq. (2) and on the incoming water flux velocity as the boundary condition, provides "finite" amplitude of the deflections at resonance frequencies despite the absence of dissipative terms in the equations of the model. In other words, both fixed amplitude of the velocity of incoming seawater flux and incompressible fluid in sub-ice-shelf area, inhibit the deflections and define the amplitude of the deflections firmly.

The comparison of the two models reveals visible distinction in the deflection profiles for tidal forcing. The distinction in the deflection profiles obtained by the two models considered here, emerges in the positions of the maxima of the deflections. The deflection maximum locus changing with ice-shelf length variation in the defection profiles obtained by the developed model (Fig. 2a), but the maximum locus becomes unchanged in the profiles obtained by the Holdsworth & Glynn model (Fig. 2b). More detailed investigation of the models shows that the distinction can be associated with different sub-ice-shelf pressure perturbations as the

response to the different forcings: (a) the forcing in the form of pressure perturbation at the ice-shelf terminus or (b) the forcing in the form of incoming seawater flux. More exactly, the Holdsworth & Glynn model provides higher pressure perturbations, than the model based on the incoming seawater flux. In other words, the model based on the pressure perturbations on the ice-shelf terminus provides higher flexural moment, which forces the ice-shelf plate become more deflected.

Moreover, the thin plate Helmholtz function (Helmholtz free energy) and the thin plate equilibrium equation, which results from the Helmholtz function [17] and on which the ice-shelf deflection models are based, imply some assumptions about the stress tensor (Cauchy stress tensor). Exactly, the three stress components σ_{xz}, σ_{yz}, σ_{zz} are approximately assumed equal to zero [17]. This assumption provides simple relations between thin plate deflections and deformation tensor components that implies a specific type of the above mentioned Helmholtz function [17], that is the following

$$\widetilde{A} = \frac{1}{2} D \iint \left\{ \left(U''_{xx} + U''_{yy} \right)^2 + 2\left(1-\nu\right) \left[\left(U''_{xy} \right)^2 - U''_{xx}\, U''_{yy} \right] \right\} dx\, dy\,, \tag{9}$$

where D is the rigidity coefficient, and the plate equilibrium equation becomes $D\,\Delta^2 U = P$. The full model considers a common elastic medium deformation, which implies that there is a distinction in the deformations of different horizontal layers in the medium. Thus, the three stress components σ_{xz}, σ_{yz}, σ_{zz} are non-zero. This forcing complementary hampers the deflections of the plate. In other words, the plate described by the full model is anticipated to be more rigid in comparison with the thin plate, which is described by the thin plate model. Thus, the distinction in the flexures profiles can be explained within the framework of the basic theory of thin plate small deflections. Moreover, the explanation of the preliminary results in [30] and of the disagreement with the results obtained by the Holdsworth and Glynn model can be sought in this distinction in the approaches of the two models - full model and thin plate model.

The ice-shelf response obtained in the harmonic history of the forcing, is symmetric and is defined by equal inflowing and outflowing seawater fluxes in the harmonic history of the forcing (Fig. 5).

Generally speaking, the amplitude of the velocity of incoming seawater flux should depend on the frequency of the incident wave. If the amplitude of the flux velocity is fixed, i.e. if we neglect the dependence on the frequency, the amplitude spectral distribution reveal weakly monotone increasing trend (Fig. 7). Nevertheless, the main result is the existence of the resonance peaks in the high-freq part of the spectrum. The resonance effects are confirmed by the experiments performed by the model of Holdsworth & Glynn for elastic beam. However, the eigen-frequencies are distinguished because the models differ in the basic equations and in the sets of boundary conditions. In particular, for ice shelf, which extends for 4 km, eigen-frequencies that were derived from the spectral distribution (Fig. 7c), are $\omega_0 \approx 1.6 \cdot 10^{-3}\ Hz$ ($T_0 \approx 630\,s$), $\omega_1 \approx 6.3 \cdot 10^{-3}\ Hz$ ($T_1 \approx 158 s$), $\omega_2 \approx 1.7 \cdot 10^{-2}\ Hz$

($T_2 \approx 60 s$). The same three eigen-frequencies, that can be obtained in the eigen-value problem in the 1D model of Holdsworth & Glynn, are $\omega_0 \approx 2.03 \cdot 10^{-3}\ Hz$ ($T_0 \approx 492 s$), $\omega_1 \approx 5.9 \cdot 10^{-3}\ Hz$ ($T_1 \approx 167 s$), $\omega_2 \approx 1.12 \cdot 10^{-2}\ Hz$ ($T_2 \approx 88 s$), respectively.

The phenomenon, which is known as "beats" and which accompanies with resonance effects, can be observed in the ice-shelf deflection histories, obtained by both the Holdsworth & Glynn model and the full model (Fig. 9). The main history, which occurs at the frequency of the forcing (of incident wave), is modulated by the history with a low frequency $\Omega << \omega$. For example, the modulating frequency is $\Omega \approx 7.5\omega$ in the Holdsworth & Glynn model (Fig. 9,a) and is $\Omega \approx 6.5\omega$ in the full model (Fig. 9,b), respectively, for the forcing frequency $\omega = 0.01\ Hz$ ($T = 100 s$).

Several of the obtained eigen-frequencies fall into infragravity part of the spectrum - the range of the frequencies of incident ocean waves that are observed in Antarctica. The term "infragravity" was introduced in [1] and means the frequencies ranging from 0.004 Hz to 0.02 Hz. The investigation of IG-wave impact on the Ross Ice Shelf [1] reveals that the rms amplitude of IG wave is about a factor 3 greater than swell and this factor increases to about 15 when sea-ice is present. The results obtained in this manuscript allow to conclude that the maximum of the amplitude of ice-shelf deflections in the infragravity spectrum can be directly associated with the resonance effect.

Finally, the full elastic model reveals that the modelled ice-shelf response to the pressure perturbation is inconsistent with the expected response, which should be in agreement in the amplitude of vibrations with the amplitude of the incident wave in a non-resonant case. The realistic results that in agreement with observations of ice-shelf flexures (in the pointed meaning), can be obtained by the full model with a little alteration in this model. The alteration means a return to the continuity equation and to the Euler equation instead of the channel wave equation in the general statement of the problem. The boundary condition at the open side of the channel is replaced by the history of seawater flux velocity instead of pressure perturbations history, respectively.

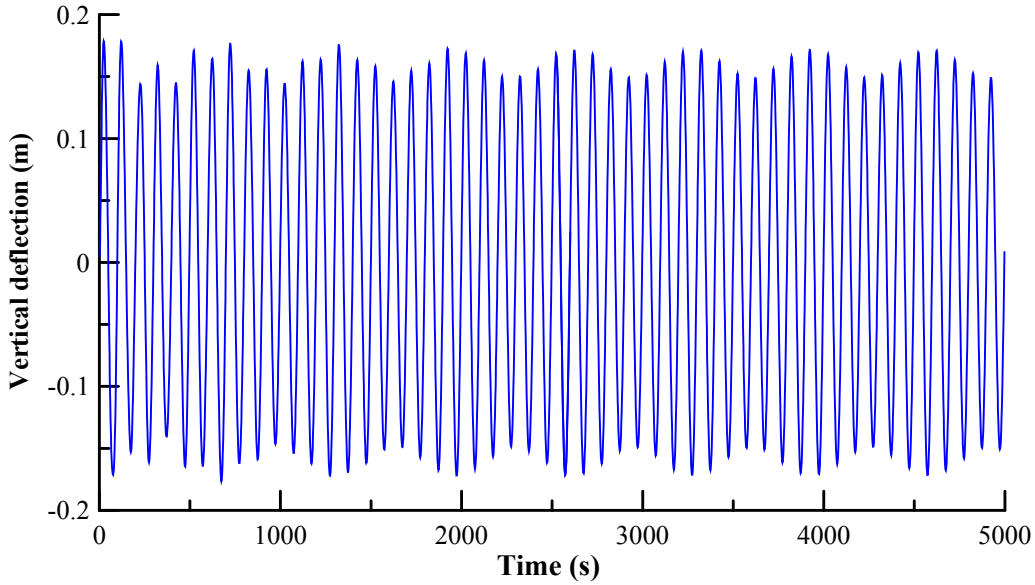

Fig. 9a

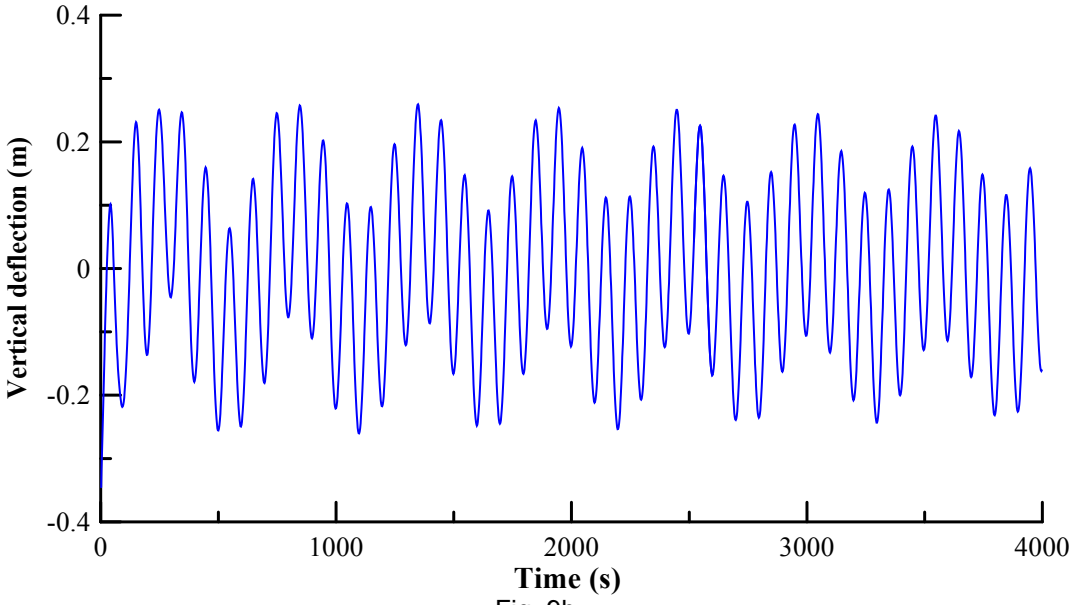

Fig. 9b

Fig. 9. Histories of ice-shelf terminus deflections obtained (a) by the Holdsworth & Glynn model (b) by the model developed in this manuscript. Young's modulus $E = 9$ GPa, Poisson's ratio $\nu = 0.33$, period of the vibrations $T = 100\,s$, incident wave amplitude $A = 1\,m$, incoming flux velocity amplitude $v_0 = 0.1\,m/s$

5. CONCLUSIONS

The full elastic model based on the coupling of continuity equation with the Euler equation that are applied in the model instead of the channel wave equation for sub-ice-shelf seawater flux, provides a good agreement between the amplitudes (i) of the modelled ice-shelf vibrations and (ii) of the incident ocean wave (in a non-resonant case). The boundary condition at the open side of the channel is replaced by the history of seawater flux velocity instead of pressure perturbations history, respectively.

The spectral amplitude distribution reveals resonance peaks that emerge in the high-freq part of the ocean wave spectrum. The model, which based on the continuity equation for the sub-ice-shelf seawater flux, provides "finite" amplitude of the deflections at resonance frequencies despite the absence of dissipative terms in the equations of the model.

Some of the resonance peaks fall into the "infragravity" part of the spectrum, which extends from 0.004 Hz to 0.02 Hz [1]. Thus, the results of the modelling allow to explain the maximum of ice-shelf deflections in the infragravity spectrum, which was observed on the Ross Ice Shelf [1]. The explanation can be found in the existence of the resonance on these high frequencies in the system, which includes glacier, ice shelf and sub-ice-shelf seawater.

NOTATION

A	the amplitude of the incident ocean wave, m
d_0	depth of the sub-ice-shelf channel, m
E	Young's modulus
g	gravitational acceleration, 9.8 m s^{-2}
H	ice thickness, m
h_s	ice surface elevation, m
h_b	ice bed elevation, m
$L\,;L_{Gl}\,;L_{Sh}$	full ice vertical cross-section length; glacier length; ice shelf length, m
T	period of incident ocean wave/period of ice shelf vibrations, s
U	horizontal deflection of ice, m
v	horizontal sub-ice-shelf water velocity, m/s
v_0	the amplitude of the incoming sea water flux velocity, m/s
W	vertical deflection of ice, m
x	horizontal axis along a flow line, m
z	vertical axis pointing upward ($z=0$ at sea level), m
ν	Poisson's ratio
$\rho\,;\rho_w$	ice density, 900 kg m^{-3}; sea water density, 1030 kg m^{-3}
σ_{ik}	stress tensor components, Pa
ω	frequency of incident ocean wave/ frequency of ice shelf vibrations, Hz

ACKNOWLEDGEMENTS

Author is grateful to Dr. G. Hilmar Gudmundsson and to prof. O.V. Nagornov for helpful comments to the manuscript. Author is grateful to Prof. J.A. Dowdeswell et al. for the data that have been used in the manuscript.

COMPETING INTERESTS

Author has declared that no competing interests exist.

REFERENCES

1. Bromirski PD, Sergienko OV, MacAyeal DR. Transoceanic infragravity waves impacting Antarctic ice shelves. Geophys. Res. Lett. 2009;37:L02502, doi:10.1029/2009GL041488.
2. Goodman DJ, Wadhams P, Squire VA. The flexural response of a tabular ice island to ocean swell. Ann. Glaciol. 1980;1:23–27.
3. Holdsworth G, Glynn J. Iceberg calving from floating glaciers by a vibrating mechanism. Nature. 1978;274:464-466.
4. Meylan M, Squire VA, Fox C. Towards realism in modelling ocean wave behavior in marginal ice zones. J. Geophys. Res. 1997;102(C10):22981–22991.
5. Squire VA, Dugan JP, Wadhams P, Rottier PJ, Liu AK. Of ocean waves and sea ice. Annu. Rev. Fluid Mech. 1995;27:115–168.
6. Turcotte DL, Schubert G. Geodynamics. 2nd ed. Cambridge: Cambridge University Press; 2002.
7. Wadhams P. The seasonal ice zone. In: Untersteiner N, editor. The geophysics of sea ice. New York: Plenum Press; 1986;825–991.
8. Bassis JN, Fricker HA, Coleman R, Minster J-B. An investigation into the forces that drive ice-shelf rift propagation on the Amery Ice Shelf, East Antarcyica. J. of Glaciol. 2008;54(184):17-27.
9. MacAyeal DR, Okal EA, Aster RC, Bassis JN, Brunt KM, Cathles LM, Drucker R, Fricker HA, Kim Y-J, Martin S, Okal MH, Sergienko OV, Sponsler MP, Thom JE. Transoceanic wave propagation links iceberg calving margins of Antarctica with storms in tropics and Northern Hemisphere. Geophys. Res. Lett. 2006;33:L17502, doi:10.1029/2006GL027235.
10. Vaughan DG. Tidal flexure at ice shelf margins. J. Geophys. Res. 2002;100(B4):6213-6224.
11. Reeh N, Christensen EL, Mayer C, Olesen OB. Tidal bending of glaciers: a linear viscoelastic approach. Ann. Glaciol. 2003;37:83–89.
12. Gudmundsson GH. Ice-stream response to ocean tides and the form of the basal sliding law. The Cryosphere. 2011;5:259–270.
Available: http://www.the-cryosphere.net/5/259/2011/
13. Sergienko OV. Elastic response of floating glacier ice to impact of long-period ocean waves. J. Geophys. Res. 2010;115:F04028, doi:10.1029/2010JF001721.
14. Dowdeswell JA, Bassford RP, Gorman MR, Williams M, Glazovsky AF, Macheret YY, Shepherd AP, Vasilenko YV, Savatyuguin LM, Hubberten H-W, Miller H. Form and flow of the Academy of Sciences Ice Cap, Severnaya Zemlya, Russian High Arctic. J. Geophys. Res. 2002;107(B4):1-15, doi:10.1029/2000JB000129.
15. Hutter K, Jöhnk K. Continuum Methods of Physical Modeling. Springer; 2004.
16. Lamb H. Hydrodynamics. 6th ed. Cambridge University Press; 1994.

17. Landau LD, Lifshitz EM. Theory of Elasticity. Vol. 7. 3rd ed. Butterworth-Heinemann; 1986.
18. Lurie AI. Theory of Elasticity. Springer; 1999.
19. Cuffey K, Paterson WSB. The physics of glaciers. 4th ed. Elsevier; 2010.
20. Konovalov YV. Inversion for basal friction coefficients with a two-dimensional flow line model using Tikhonov regularization. Research in Geophysics. 2012;2:e11:82-89. Available: http://dx.doi.org/10.4081/rg.2012.e11.
21. Blatter H. Velocity and stress fields in grounded glaciers: a simple algorithm for including deviatoric stress gradients. J. Glaciol. 1995;41:333–344.
22. Blatter H, Clarke GKC, Colinge J. Stress and velocity fields in glaciers: Part II. Sliding and basal stress distribution. J. Glaciol. 1998;44:457–466.
23. Colinge J, Blatter H. Stress and velocity fields in glaciers: Part I. Finite difference schemes for higher-order glacier models. J. Glaciol. 1998;44:448–456.
24. Hindmarsh RCA, Hutter K. Numerical fixed domain mapping solution of free surface flows coupled with an evolving interior field. Int. J. Numer. Anal. Methods Geomech. 1988;12:437-459.
25. Hindmarsh RCA, Payne AJ. Time-step limits for stable solutions of the ice sheet equation. Ann. Glaciol. 1996;23:74-85.
26. Pattyn F. Ice-sheet modeling at different spatial resolutions: focus on the grounding zone. Ann. Glaciol. 2000;31:211-216.
27. Pattyn F. Transient glacier response with a higher-order numerical ice-flow model. J. Glaciol., 2002;48(162):467-477.
28. Pattyn F. A new three-dimensional higher-order thermomechanical ice sheet model: Basic sensitivity, ice stream development, and ice flow across subglacial lakes. J. Geophys. Res. 2003;108(B8),2382, doi:10.1029/2002JB002329.
29. Schulson EM. The Structure and Mechanical Behavior of Ice. JOM. 1999;51(2):21-27.
30. Konovalov YV. Ice shelf flexures modeled with a 2-D elastic flow line model. The Cryosphere Discuss. 2011;5:2841–2863. Available: http://www.the-cryosphere-discuss.net/5/2841/2011/

Peer-review history:
The peer review history for this paper can be accessed here:
http://www.sciencedomain.org/review-history.php?iid=283&id=4&aid=2204